The Astrophysical Journal, 999:97 (15pp), 2026 March 1 https://doi.org/10.3847/1538-4357/ae32f2

Measuring the Central Dark Mass in NGC 4258 with JWST/NIRSpec Stellar Kinematics

Dieu D. Nguyen[1], Hai N. Ngo[2], Michele Cappellari[3], Tinh Q. T. Le[4], Tien H. T. Ho[2], Tuan N. Le[5], Elena Gallo[1], Niranjan Thatte[3], Fan Zou[1], Michele Perna[6], and Miguel Pereira-Santaella[7]

[1] Department of Astronomy, University of Michigan, 1085 South University Avenue, Ann Arbor, MI 48109, USA; dieun@umich.edu
[2] Faculty of Physics and Engineering Physics, University of Science, Vietnam National University in Ho Chi Minh City, Vietnam
[3] Sub-Department of Astrophysics, Department of Physics, University of Oxford, Denys Wilkinson Building, Keble Road, Oxford, OX1 3RH, UK
[4] Department of Physics, International University, Vietnam National University in Ho Chi Minh City, Vietnam
[5] International Centre for Interdisciplinary Science and Education, 07 Science Avenue, Ghenh Rang, 55121, Quy Nhon, Vietnam
[6] Centro de Astrobiología (CAB), CSIC—INTA, Departamento de Astrofísica, Cra. de Ajalvir Km. 4, 28850—Torrejón de Ardoz, Madrid, Spain
[7] Instituto de Física Fundamental, CSIC, Calle Serrano 123, 28006 Madrid, Spain

Received 2025 September 23; revised 2025 December 10; accepted 2025 December 30; published 2026 February 25

Abstract

We present a new stellar-dynamical measurement of the supermassive black hole (SMBH) mass in the nearby spiral galaxy NGC 4258 (M106), a critical benchmark for extragalactic mass measurements. We use archival James Webb Space Telescope (JWST) Near-Infrared Spectrograph (NIRSpec) integral field unit data (G235H/F170LP grating) to extract high-resolution two-dimensional stellar kinematics from the CO bandhead absorption features within the central $3'' \times 3''$. We extract the stellar kinematics after correcting for instrumental artifacts and separating the stellar light from the nonthermal active galactic nucleus (AGN) continuum. We employ Jeans anisotropic models to fit the observed kinematics, exploring a grid of 12 models to systematically test the impact of different assumptions for the point-spread function, stellar mass-to-light ratio profile, and orbital anisotropy. All 12 models provide broadly acceptable fits, albeit with minor differences. The ensemble median and 68% (1σ) bootstrap confidence interval of our 12 models yield a black hole mass of $M_{\rm BH} = (4.08^{+0.19}_{-0.33}) \times 10^7\,M_\odot$. This paper showcases the utility of using the full model ensemble to robustly account for systematic uncertainties, rather than relying on formal errors from a single preferred model, as has been common practice. Our result is just 5% larger than, and consistent with, the benchmark SMBH mass derived from water-maser dynamics, validating the use of NIRSpec stellar kinematics for robust SMBH mass determination. Our analysis demonstrates JWST's ability to resolve the SMBH's sphere of influence and deliver precise dynamical masses, even in the presence of significant AGN continuum emission.

Unified Astronomy Thesaurus concepts: Astrophysical black holes (98); Galaxy kinematics (602); Galaxy dynamics (591); Galaxy nuclei (609); Galaxy spectroscopy (2171); Astronomy data modeling (1859)

Materials only available in the online version of record: machine-readable table

1. Introduction

NGC 4258 (M106) is a nearby spiral galaxy of Hubble type SABbc, located at a distance $D = 7.2 \pm 0.3$ Mpc, the most precise extragalactic distance measured (J. R. Herrnstein et al. 1999). It hosts one of the closest known active galactic nuclei (AGN) with a nuclear nonstellar continuum and broad optical emission lines detected in polarized light (B. J. Wilkes et al. 1995), consistent with the presence of an obscured central engine. This galaxy is particularly notable for containing one of the best-constrained supermassive black hole (SMBH) masses ($M_{\rm BH}$) in the nearby Universe (M. Miyoshi et al. 1995). Using very-long-baseline interferometry observations of a rotating water-maser disk within 0.13 pc of the nucleus, a precise dynamical mass of $M_{\rm BH}^{\rm maser} = (3.9 \pm 0.1) \times 10^7\,M_\odot (D/7.2\,{\rm Mpc})$ was determined (J. R. Herrnstein et al. 1999). Aside from Sgr A* in the Milky Way, whose mass has been dynamically measured from the full orbits of individual stars via optical observations (R. Genzel et al. 1996; A. M. Ghez et al. 1998), NGC 4258 remains the most precisely measured extragalactic $M_{\rm BH}$ to date. It serves as a critical benchmark for calibrating other $M_{\rm BH}$ estimation methods.

Several previous studies have explored the SMBH in NGC 4258 using a variety of observational data and dynamical modeling approaches. These include (i) refined maser dynamical modeling (J. R. Herrnstein et al. 2005); (ii) long-slit gas kinematics from the Hubble Space Telescope (HST) Space Telescope Imaging Spectrograph (STIS), modeled under the assumption of circular motion in a thin ionized gas disk, yielding $M_{\rm BH,gas} = (7.9^{+2.5}_{-1.4}) \times 10^7\,M_\odot$ (G. Pastorini et al. 2007, converted to 1σ confidence); (iii) stellar kinematics based on the Ca II triplet (CaT, at $\sim$0.854 μm) absorption lines from HST/STIS and orbit-based modeling using the M. Schwarzschild (1979) method, resulting in $M_{\rm BH,stars} = (3.3 \pm 0.2) \times 10^7\,M_\odot$ (C. Siopis et al. 2009); and (iv) stellar kinematics derived from CO bandhead absorption features at $\sim$2.3 μm using the Gemini Near-Infrared Integral-Field Spectrograph (NIFS) and modeled with Jeans anisotropic models (JAMs; M. Cappellari 2008, 2020), giving $M_{\rm BH,stars} = (4.8 \pm 0.3) \times 10^7\,M_\odot$ (converted to 1σ confidence; D. A. Drehmer et al. 2015). These results are consistent with the maser-based estimate (M. Miyoshi et al. 1995; J. R. Herrnstein et al. 2005) within their quoted uncertainties.

Given the SMBH mass inferred from maser disk dynamics and adopting a bulge velocity dispersion of $\sigma \approx 105\,\mathrm{km\,s^{-1}}$ (D. A. Drehmer et al. 2015), the SMBH's radius of the sphere of influence (SOI)[8] is estimated as $r_{\rm SOI} \approx 15$ pc. Assuming a flat Lambda cold dark matter (ΛCDM) cosmology ($H_0 \approx 70$ km s^{-1} Mpc^{-1}, $\Omega_{\rm m,0} \approx 0.3$, and $\Omega_{\Lambda,0} \approx 0.7$), the corresponding angular scale is 35 pc$''^{-1}$, implying $r_{\rm SOI} \approx 0\farcs42$. This is 2–3 times larger than the point-spread function (PSF) full width at half-maximum of the James Webb Space Telescope (JWST) Near-Infrared Spectrograph (NIRSpec), which has a FWHM of$_{\rm PSF} \approx 0\farcs15 - 0\farcs18$ at 2.4 μm (F. D'Eugenio et al. 2024).

In this work, we analyze the stellar kinematics of the nuclear region of NGC 4258 using archival JWST/NIRSpec data (PID: 02016, PI: Anil C. Seth) in combination with JAMs to constrain the dynamical properties of the system. By employing the JAM framework (e.g., D. D. Nguyen 2017; D. D. Nguyen et al. 2017; C. P. Ahn et al. 2018; D. D. Nguyen et al. 2018, 2019; T. A. Davis et al. 2020; D. D. Nguyen et al. 2025a), we explore how variations in key model parameters, such as inclination (i), velocity anisotropy, and stellar mass-to-light ratio (M/L), influence the modeled kinematics and the inferred SMBH mass in NGC 4258. This work represents the fourth dynamical black hole mass measurement obtained with JWST/NIRSpec, following the initial results for NGC 4736 (D. D. Nguyen et al. 2025b), NGC 4486B (B. Tahmasebzadeh et al. 2025), and UCD 736 (M. A. Taylor et al. 2025). Together, these studies demonstrate NIRSpec's capability to deliver high-quality stellar kinematics and robust dynamical black hole masses.

This paper is organized as follows. In Section 2, we describe the JWST/NIRSpec observations, the reduction of the integral field unit (IFU) data, the wiggles correction for a few central spectra, and the extraction of the two-dimensional (2D) line-of-sight velocity distribution (LOSVD) from the "gold-standard" stellar CO bandhead absorption features. In Section 3, we combine this 2D LOSVD with the stellar photometric data from D. A. Drehmer et al. (2015) as input for the JAM modeling to determine the mass of the central SMBH in NGC 4258. We present and discuss our results, along with concluding remarks, in Sections 4 and 5, respectively.

2. Observations and Kinematics

2.1. JWST/NIRSpec IFU

The NIRSpec G235H/F170LP observation of NGC 4258 was obtained on 2023 February 15, and comprises eight exposures of 218.8 s each, yielding a total on-source integration time of 1750.7 s. The observations were conducted in high-spectral-resolution mode ($R \sim 2700$), covering the wavelength range of 1.66–3.05 μm. The NRSIRS2RAPID readout pattern was used, with 14 groups per integration, one integration per exposure, and a four-point medium-cycling dither pattern. Data reduction followed the standard JWST calibration pipeline for NIRSpec IFU data, using STScI pipeline version 1.14.0 and Calibration Reference Data System (CRDS) context 1063.[9] The final IFU data cube has a spatial pixel scale of 0.″1, approximately 4 times smaller than the SMBH's $r_{\rm SOI}$ if assuming the maser dynamical SMBH mass (Section 1), and extends within a field of view (FOV) of $3'' \times 3''$.

2.2. Wiggles Corrections

The spatial undersampling of the NIRSpec PSF produces characteristic fluctuations, commonly referred to as "wiggles," in the single-spaxel spectra of bright targets. The effect is significantly reduced when integrating over apertures larger than ~0.″2–0.″5 (e.g., D. R. Law et al. 2023). To mitigate this effect in our data cubes, we apply the correction algorithm developed by M. Perna et al. (2023),[10] which provides an empirical approach to remove wiggles in the absence of a dedicated correction in the standard NIRSpec pipeline. Below, we briefly summarize the main steps of the procedure; we refer the reader to M. Perna et al. (2023) for full technical details.

We model the wiggles as a sinusoidal function in the spectrum extracted from the brightest spaxel of the cube, where the wiggles are most prominent across the entire spectral range, as shown in Figure 1. Prior to fitting, we mask prominent emission and absorption features, as well as the spectral gap between the two NIRSpec detectors, to avoid contaminating the model with intrinsic spectral features. The modeling of a sinusoidal function is applied iteratively in rolling windows across the spectral range, allowing the model to adapt locally to wavelength-dependent variations. The model is tuned such that the corrected single-spaxel spectrum closely matches the spectrum extracted from a larger aperture, where the wiggles are averaged out. For our targets, we use a circular aperture of 4 pixel radius (0.″4), centered on the peak of the collapsed (white-light) image. We verify that this aperture is sufficient to suppress the wiggles in our datasets. The wiggle frequency derived from this reference spectrum is then adopted as a prior for modeling and subtracting the wiggles in other spaxels where the effect is evident. The IFU data cube corrected for wiggles is used in all subsequent analyses.

2.3. NIRSpec PSF

This work will test the impact of our synthetic NIRSpec PSFs at 2.4 μm on the $M_{\rm BH}$ measurement in NGC 4258, in addition to the adopted single-Gaussian PSF (FWHM$_{\rm PSF,tot} = 0\farcs15 - 0\farcs18$) from F. D'Eugenio et al. (2024, 2026).

To generate the synthetic NIRSpec PSFs, we used `stpsf` (M. Perrin et al. 2025; `stpsf` replaces `WebbPSF`).[11] We used the following parameters: instrument NIRSpec, mode IFU, disperser G235H, filter F170LP, and wavelength 2.3 μm. `stpsf` generates PSFs with native detector sampling and factor 4 oversampling, both with and without additional instrumental effects (distortion, detector crosstalk, etc). For our analysis, we used the `DET_DIST` extension that incorporates the additional instrumental effects, with factor 4 oversampling.

We constructed oversampled synthetic PSF models from extensions 1 and 3 using the multi-Gaussian expansion (MGE; E. Emsellem et al. 1994; M. Cappellari 2002) via the MGE_FIT_SECTOR routine in the MGEFIT package (M. Cappellari 2002).[12] For both extensions, we adopted a fixed number of three Gaussians, ensuring each Gaussian fit well with the

[8] The spherical region surrounding the black hole, where its gravitational potential dominates and the enclosed stellar mass equals approximately twice the black hole mass, can be estimated as $r_{\rm SOI} \approx GM_{\rm BH}/\sigma^2$, where G is the gravitational constant.

[9] https://jwst-crds.stsci.edu

[10] https://github.com/micheleperna/JWST-NIRSpec_wiggles

[11] v2.0.0: https://github.com/spacetelescope/stpsf

[12] v5.0: https://pypi.org/project/mgefit/

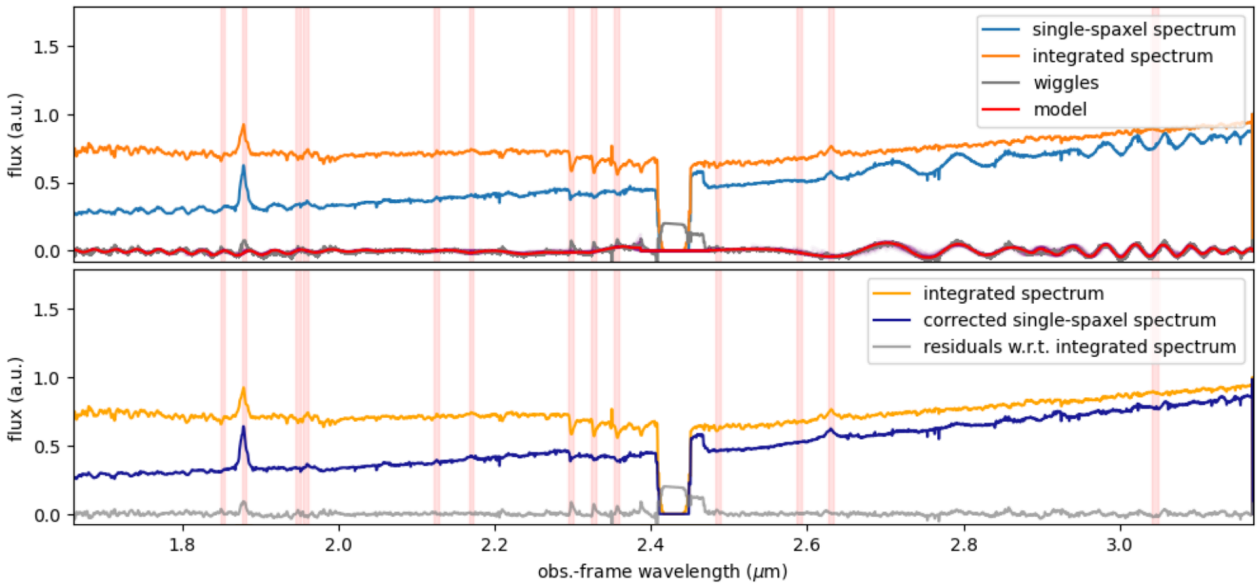

Figure 1. Modeling of the wiggles in single-spaxel spectra for NGC 4258. Top panel: the integrated spectrum (orange), single-spaxel spectrum (blue), and residual wiggles (gray). The red curve shows the best-fit model to the wiggles. Bottom panel: the corrected single-spaxel spectrum (dark blue), compared to the integrated spectrum (orange); the gray curve shows the residuals after correction. In all panels, red shaded regions indicate emission lines excluded from the fit.

data at its position. Additionally, we allowed a free number of Gaussians when fitting extension 3, resulting in a total FWHM of $\approx 0\farcs15$, fully consistent with the empirical estimate from F. D'Eugenio et al. (2026). All three synthetic MGE PSF models are summarized in Table 1.

2.4. Stellar Kinematics Templates and pPXF Setup

Since the nuclear spectra of NGC 4258 are dominated in several central spaxels by AGN continuum emission (B. J. Wilkes et al. 1995; after applying wiggles correction, as in Section 2.2), care must be taken in the stellar kinematics extraction. The AGN continuum itself does not bias the kinematics, but it dilutes the stellar CO bandhead absorption features of cool, evolved giant stars that are used to derive the stellar velocity dispersion σ. This dilution reduces the measured line strength γ and, if uncorrected, could lead to underestimates of σ (see Section 2.2 of R. P. van der Marel & M. Franx 1993, for the strong correlation between σ and γ). In addition, the rising AGN continuum could be mistaken for a stellar population change, distorting the template mix and introducing systematic errors. To avoid these issues, it is essential to include an additive polynomial in the spectral fits to account for the smooth AGN continuum component while preserving the stellar absorption features (M. Cappellari et al. 2009).

For clarity, the observed line strength γ can be defined as the stellar flux fraction, $\gamma = \mathrm{stars}/(\mathrm{stars}+\mathrm{AGN})$, i.e., the ratio between the flux contributed by the best-fitting stellar template alone and the observed mean flux in the fitted spectral range. Intuitively, $\gamma \approx 1$ in regions far from the nucleus where the AGN contribution is negligible, and it decreases below unity toward the center, dropping substantially in the few spaxels where the AGN continuum dominates.

In this work, we extracted 2D stellar kinematic maps from the NIRSpec G235H/F170LP data cube of NGC 4258 using the CO bandhead absorption features (e.g., M. Cappellari et al. 2009; D. D. Nguyen et al. 2014, 2023; S. Thater et al. 2023) and the Penalized PiXel-Fitting (PPXF) method (M. Cappellari & E. Emsellem 2004; M. Cappellari 2017, 2023).[13] To evaluate the robustness of our results and quantify template-related systematics, we employed both the empirical X-shooter Spectral Library (XSL) Data Release 3 (DR3; 830 spectra from 683 stars; K. Verro et al. 2022)[14] and the PHOENIX synthetic stellar library (T.-O. Husser et al. 2013).[15]

The XSL DR3 library covers the full wavelength range of the X-shooter spectrograph (3000–25000 Å) with a spectral resolution of $R \approx 10{,}000$, and has been corrected for dust extinction. It includes a wide variety of stellar types, from O to M, including asymptotic giant branch stars, and spans most of the Hertzsprung–Russell diagram. In contrast, the PHOENIX library, generated using the spherical mode of PHOENIX, which includes the effects of microturbulence in stellar atmospheres, offers significantly higher spectral resolution ($R \approx 500{,}000$ in the optical and near IR, $R \approx 100{,}000$ in the IR and $\Delta\lambda = 0.1$ Å), extends from 0.3 to 5 μm, and is free from telluric absorption gaps. It spans a broad range of stellar parameters: $2300\,\mathrm{K} \leqslant T_{\rm eff} \leqslant 25{,}000\,\mathrm{K}$, $0.0 \leqslant \log(g) \leqslant +6.0$, $-4.0 \leqslant [\mathrm{Fe/H}] \leqslant +1.0$, and $-0.2 \leqslant [\alpha/\mathrm{Fe}] \leqslant +1.2$.

The XSL will be adopted throughout the main text as our fiducial template unless otherwise noted.

2.5. Determining the Optimal Stellar Template

To separate the stellar light from the nonthermal AGN continuum in the NIRSpec G235H/F170LP spectra of NGC 4258, we need a fixed optimal XSL template for all spatial positions to ensure an unbiased extraction of stellar kinematics (A. Marconi et al. 2000; J. D. Silge & K. Gebhardt 2003). Since there is no clear evidence of nuclear stellar population variation (C. Siopis et al. 2009), we assumed the fixed optimal XSL template and modeled the nonthermal AGN continuum using both multiplicative and additive Legendre polynomials (e.g., D. A. Simon et al. 2024) within PPXF. We

[13] v8.2.1: https://pypi.org/project/ppxf/
[14] http://xsl.u-strasbg.fr
[15] http://phoenix.astro.physik.uni-goettingen.de

carefully experimented with different combinations of the degrees of the multiplicative and additive Legendre polynomials and adopted as our preferred approach a fit with `mdegree = 4` and `degree = 4`, allowing for variations in stellar line strength with radius and accounting for residual sky-subtraction errors, spectral calibration imperfections, and AGN contamination. The polynomials account for low-order variations in line strength and potential instrumental effects, allowing velocity dispersion to be reliably measured for a few central spaxels (e.g., $0\farcs1 - 0\farcs3$), before AGN photon noise overwhelms the stellar signal (e.g., M. Cappellari et al. 2009).

To obtain a global spectrum, we combined all spaxel spectra within an annular region from $0\farcs4$ to $1\farcs4$ centered on the centrally brightest pixel (outlined by the two red rings in the left panel of Figure 2), excluding the central spaxels that are strongly contaminated by AGN continuum emission. This annular spectrum achieves a signal-to-noise ratio (S/N) of 215 per spectral pixel. Prominent emission lines were masked, and the spectrum was logarithmically rebinned along the spectral dimension using a constant velocity scale by setting `velscale = 50` $\mathrm{km\,s^{-1}\,pixel^{-1}}$, as calculated using Equation 8 of M. Cappellari (2017). Next, we took into account the instrumental broadening in the XSL template by convolving the XSL template with a Gaussian whose dispersion is defined as the differential Gaussian dispersion between the template spectra and the global spectrum (see Equation (5) of M. Cappellari 2017). Here, when deriving the fixed optimal XSL template, we adopt a constant Gaussian. However, when deriving the kinematic bins across the NIRSpec FOV (Section 2.7), where the line broadening may vary spatially and spectrally, we convolve the XSL template with a spatial- and wavelength-dependent line-spread function (e.g., D. D. Nguyen et al. 2018) derived by D. D. Nguyen et al. (2025b, Appendix B).

We then applied PPXF to fit this global spectrum using the XSL-instrumental-broadened spectra and a Gauss-Hermite expansion truncated at second order by setting `moments = 2`. This setup yields robust estimates of the recession velocity (V, or rotational velocity relative to the systemic velocity $V_{\rm sys}$) and velocity dispersion (σ), which are our primary kinematic quantities of interest. Modeling only V and σ avoids the need to select a bias parameter for penalizing higher-order Gauss-Hermite moments (O. E. Gerhard 1993; R. P. van der Marel & M. Franx 1993), which otherwise requires tuning via Monte Carlo simulations.

This fitting process produced a fixed optimal stellar template, defined as a linear combination of 18 giant stars' spectra. The template provides an accurate description of the spectrum from 2.200 to 2.375 μm, which contains most of the significant stellar absorption features of the CO bandheads, as seen in the right panel of Figure 2. The template is dominated by the K4III star (HD109871 of XSL), which contributes $\approx$50% of the total flux and alone provides a relatively good fit to the annular spectrum. However, additional contributions from a giant M9 star (BMB 289, $\approx$12% of the flux) and an M4 star (SHV 0535237-700720, $\approx$8% of the flux) are required to reproduce the data. This best-fit PPXF model for the integrated spectrum within an annular region of $0\farcs4 < r < 1\farcs4$ yields a stellar velocity dispersion of $\sigma = 104 \pm 4\,\mathrm{km\,s^{-1}}$ and a Heliocentric recession velocity of $V = 451 \pm 5\,\mathrm{km\,s^{-1}}$, consistent with the previously reported value for the bulge component constrained from Gemini/NIFS observations (D. A. Drehmer et al. 2015). These 1σ measurement errors were determined as the standard deviation through 200 Monte Carlo perturbation simulations of the best-fit model (D. C. Hoaglin et al. 1983; M. Cappellari & E. Emsellem 2004).

Table 1
MGE of the NIRSpec G235H/F170LP `stpsf` PSF

j	Light Fraction	σ (arcsec)	$\mathrm{FWHM}^{\rm tot}_{\rm PSF}$ (arcsec)
(1)	(2)	(3)	(4)
Extension 1 (fix number of Gaussians = 3)			
1	0.6703	0.036	0.08 (PSF 1)
2	0.0436	0.190	
3	0.0172	0.997	
Extension 3 (free number of Gaussians)			
1	0.7400	0.065	0.15 (PSF 2)
2	0.1498	0.141	
3	0.0621	0.336	
4	0.0245	0.626	
5	0.0176	0.877	
Extension 3 (fix number of Gaussians = 3)			
1	0.8592	0.083	0.20 (PSF 3)
2	0.1145	0.372	
3	0.0263	1.100	

Notes. Column (1): the number of circular Gaussian components. Column (2): the fractional light contribution of each Gaussian, normalized to unity. Column (3): the Gaussian dispersions along the major axis, in arcseconds. Column (4): the axial ratios (minor-to-major axis). Column (5): the total FWHM of the composite PSF; the FWHM of PSF 2 is consistent with the empirical NIRSpec PSF from F. D'Eugenio et al. (2024) and F. D'Eugenio et al. (2026).

2.6. Separating Stellar Light from AGN Continuum

To assess the reliability of the fixed global stellar template for extracting stellar kinematics while accounting for the nonthermal continuum, we fit high-S/N spectra constructed by coadding spaxels within concentric annuli spanning $0\farcs1$-$1\farcs7$ in the NIRSpec G235H/F170LP data cube using PPXF.

In Figure 3, we present the radial variation of the NIRSpec G235H/F170LP spectra for NGC 4258 and their corresponding best-fitting PPXF models. The measurements in the left-hand panels show the change in stellar line strength (γ) and velocity dispersion (σ) with radius, while the right-hand panels display the fractional flux contribution of the best-fitting stellar template over the same radial range. The influence of the nonstellar continuum is evident from the varying slope of the spectra. At the nucleus, the nonthermal component rises modestly, producing a nearly linear continuum in the central spaxel, where it contributes 56% of the total flux. This fraction drops rapidly to $\approx$32% at $r \approx 0\farcs1$ and falls below 23% beyond $r = 0\farcs2$. Despite this nonstellar contribution, the stellar spectrum at all radii is still well represented by the fixed, convolved stellar template after subtracting the continuum.

We quantified the dilution of stellar light by the central nonthermal continuum in Figure 4, which shows the surface-brightness profile $I(r)$ measured from the NIRSpec G235H/F170LP data cube of NGC 4258, along with the radial profile of the stellar contribution, estimated as $\Gamma(r) = I(r)\gamma(r)$ based on the PPXF fits in individual spatial bins (see Figure 4 of

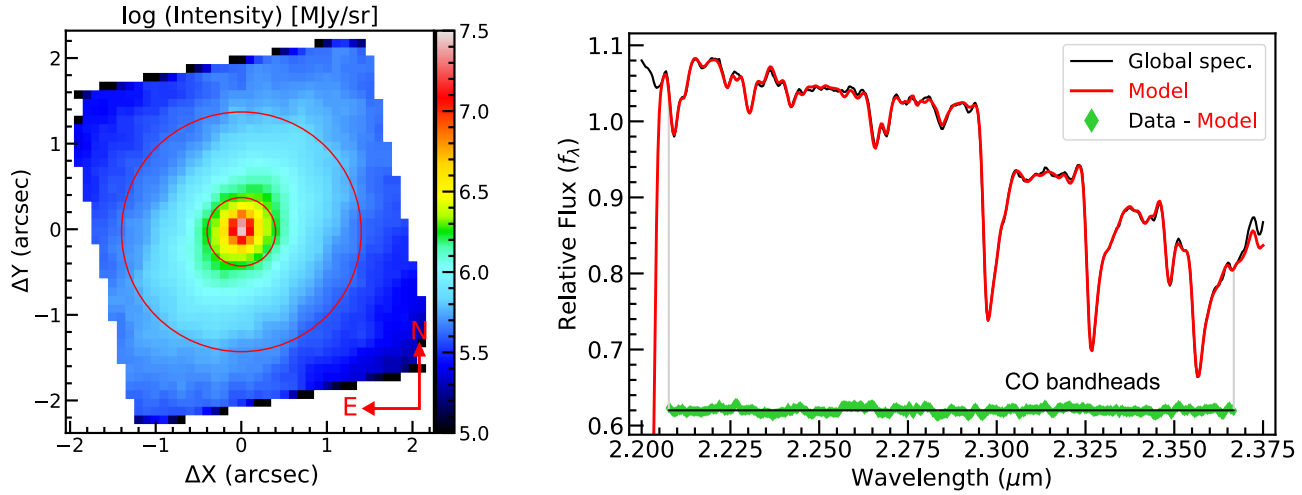

Figure 2. Left: logarithmic integrated intensity map of the NIRSpec G235H/F170LP data cube, collapsed along the spectral axis, excluding the detector gap at ∼2.41–2.49 μm. The annular region outlined by the two red rings ($0\farcs4 < r < 1\farcs4$) indicates the area from which the global spectrum was extracted. Right: optimal stellar template for NGC 4258. The observed global spectrum (black line) is compared to the broadened best-fit template obtained with PPXF (red line). The fit residuals (green points) are vertically offset by +0.62 to compress the y-axis range and better illustrate the stellar CO absorption bandheads. This same vertical offset is applied to all subsequent figures of this type.

R. P. van der Marel 1994 for M87 and Figure 6 of M. Cappellari et al. 2009 for Centaurus A). We approximated the radial stellar-light distribution with a single power-law function, $\Gamma(r) = \alpha \times r^{\beta}$ (red line), adopting $\alpha = 0.04$ and $\beta = -1.02$. This single power-law overpredicts the stellar-light fraction within $0\farcs1$ if the effect of the JWST/NIRSpec PSF at 2.3 μm is not included. To properly account for the PSF effect, we performed the following steps:

1. We generated a synthetic image with an intrinsic surface-brightness profile $\Sigma \propto r^{-1.02}$ sampled at $0\farcs025$ pixel^{-1}, i.e., oversampled by a factor of 4 relative to the native JWST/NIRSpec scale (Section 2.3).
2. We convolved this image with the synthetic JWST/NIRSpec PSF at the same sampling.
3. We rebinned the convolved image to the NIRSpec scale ($0\farcs1$ pixel^{-1}) by summing 4 × 4 spaxels.
4. We measured the stellar fraction in the central spaxel of the rebinned image.

The resulting central-stellar-fraction measurement falls along the same trend defined by the two innermost γ values as seen in Figure 4, showing that the apparent break is entirely explained by PSF convolution. Therefore, the deviation near the nucleus does not indicate a true change in the intrinsic stellar surface-brightness profile within the NIRSpec FOV, but instead reflects instrumental and sampling effects that are mitigated once the PSF is properly accounted for.

This experiment confirms that the observed radial spectral variation is consistent with weak nonthermal continuum emission and residual instrumental artifacts, rather than intrinsic changes in the stellar population. The measurement of $\gamma(r)$ enables a reliable assessment of the stellar kinematics even in the unresolved nucleus, where the stellar light is strongly diluted by AGN-related emission.

Given that stars still contribute 44% of the total flux in the central spaxel, the kinematics there are subject to larger systematic uncertainties (≈10%) but remain sufficiently reliable to be included in our dynamical modeling (Section 3.2). Beyond $r = 0\farcs1$, the stellar kinematics are robust and can be measured with uncertainties below 4%.

2.7. Two-dimensional Kinematic Maps

To derive the LOSVD maps of the nucleus of NGC 4258, we applied the adaptive Voronoi binning method (M. Cappellari & Y. Copin 2003)[16] to spatially group spaxels until reaching a target S/N = 100 per spectral pixel, resulting in $N = 403$ kinematic Voronoi bins. The chosen target S/N represents a compromise, allowing spaxels beyond $r \approx 0\farcs5 \approx r_{\rm SOI}$ to be grouped, while retaining unbinned spaxels within this radius to enable precise measurements of the stellar kinematics inside $r_{\rm SOI}$. Inside the SOI, the S/N of individual unbinned spaxels ranges from 100 to 200 per spectral pixel, increasing toward the central peak. Each binned/unbinned spectrum was resampled onto a logarithmic wavelength scale. For all bins, the PPXF fit used the fixed optimal global stellar template, convolved with the LOSVD, and included fourth-degree multiplicative and additive Legendre polynomials.

Figure 5 presents the logarithmic integrated intensity map (panel (A), the same as the left panel of Figure 2), with a marked spaxel that has the spectral fit PPXF in panel (B), as well as the resulting maps of rotational velocity V (panel (C)), velocity dispersion σ (panel (D)), rms velocity $V_{\rm rms} = \sqrt{V^2 + \sigma^2}$ (panel (E)), and stellar line strength γ (panel (F)). The nucleus exhibits modest rotation, with $|V| \approx 80 \pm 3$ km s^{-1} at the edge of the NIRSpec IFU field (after subtracting the systemic/heliocentric velocity of $v_{\rm sys} = 451 \pm 5$ km s^{-1}), and a global kinematic position angle of $\mathrm{PA_{kin}} = 147° \pm 7°$. Both $v_{\rm sys}$ and $\mathrm{PA_{kin}}$ are derived from the velocity field using the PAFIT package (D. Krajnović et al. 2006).[17] The velocity dispersion rises gradually from ∼105 ± 5 km s^{-1} at $r \gtrsim 1''$ to a sharp central peak of ∼191 ± 12 km s^{-1} within $r \lesssim 0\farcs2$, consistent with a corresponding increase in $V_{\rm rms}$ from ∼120 ± 4 km s^{-1} to ∼191 ± 12 km s^{-1} along the nucleus' major axis. This steep rise in velocity dispersion (and rms velocity) strongly supports the presence of a central SMBH. We present these stellar kinematic measurements in Table 2.

[16] v3.1.5: https://pypi.org/project/vorbin/
[17] v2.0.8: https://pypi.org/project/pafit/

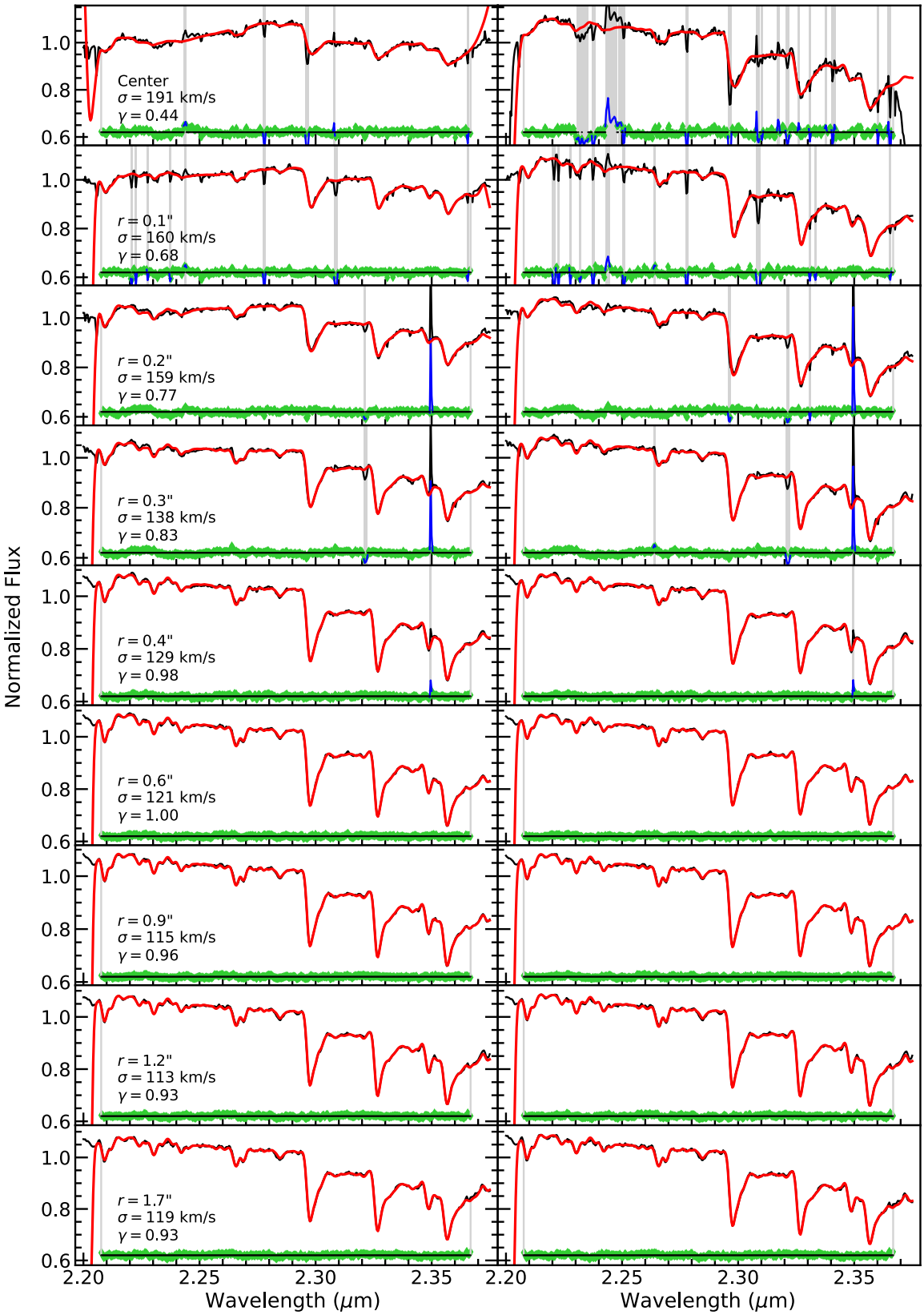

Figure 3. Radial variation in the NIRSpec G235H/F170LP spectrum of NGC 4258. Left column: Each panel shows the observed spectrum (black line), obtained by coadding spaxels within circular annuli of radius r. The best-fitting PPXF model (red line) includes the global stellar template (left panel of Figure 2, constrained from Section 2.5) convolved with a Gaussian LOSVD, plus fourth-degree multiplicative and additive polynomials, which represent the nuclear nonthermal spectrum. Residuals are shown as green dots below each fit. Spectral regions affected by emission lines or artifacts were excluded from the fit (gray areas). Right column: the global stellar template convolved with the LOSVD (red line) is compared to the observed spectrum after subtraction of the nuclear nonthermal component (black line).

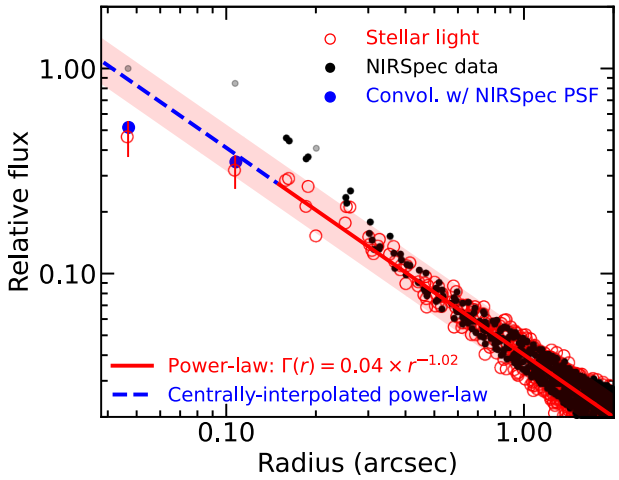

Figure 4. The radial surface-brightness profile $I(r)$, measured from individual VORONOI bins in the NIRSpec G235H/F170LP data cube of NGC 4258 (filled black dots), is compared to the estimated stellar-light profile $\Gamma(r) = I(r)\gamma(r)$ (red open circles). The underlying stellar distribution is smooth and well approximated by a single power law (red line with pink region shows its 1σ uncertainty). The PSF-convolved central interpolation of this single power law also reproduces the two innermost γ measurements, which lie below the intrinsic (unconvolved) profile, indicating that their apparent decline is fully consistent with PSF effects. The gray points represent the pixels where $\gamma < 0.5$.

We also assessed the robustness of our stellar kinematic measurements by reanalyzing the data using the synthetic PHOENIX stellar library (Section 2.4), and compared the results to those obtained with the empirical XSL library (panels (C)–(F) of Figure 5). The resulting maps are highly consistent, with differences $\lesssim$3%.

The irregular morphology of the stellar-light fraction in panel (F) of Figure 5 is not physical but is caused by residual wiggle/continuum effects and the sensitivity of γ to the adopted Voronoi binning. These small residuals introduce bin-to-bin variations in the continuum subtraction, producing the apparent patchiness and the decrease/scatter of γ in some outer bins despite their adequate S/N. Importantly, this behavior does not affect our stellar kinematic measurements. In the PPXF fits, the additive and multiplicative polynomials effectively absorb the AGN continuum and any remaining wiggle/continuum structure, preventing the known σ–γ dependency, between the velocity dispersion and the line strength of the stellar templates, and ensuring that the derived velocity dispersions are robust across the field.

Our derivation of the stellar LOSVD from the NIRSpec G235H/F170LP IFU data is consistent with the Gemini/NIFS measurements of D. A. Drehmer et al. (2015). The central $V_{\rm rms}$ from NIRSpec is $\approx$11 km s^{-1} higher than the NIFS value; this small difference is unsurprisingly given the substantially different PSFs of JWST/NIRSpec and Gemini/NIFS, which change the amount of central velocity smoothing and can produce modest systematic differences in $V_{\rm rms}$.

2.8. Defining the Galaxy Center

We identified the photometric AGN-aligned center by computing the weighted barycenter of the $\sim$100 brightest pixels. Unlike the kinematic center, which is less accurately determined because it relies on LOSVD extractions (Section 2.7), the photometric center can be measured with much higher precision. Given that the black hole is expected to coincide with the surface-brightness center, we therefore adopted the photometric AGN-aligned center to define the origin of our models, and this choice is reflected in all figures.

3. Dynamical Modeling

3.1. Stellar Mass Model

The surface brightness of NGC 4258 was carefully modeled by D. A. Drehmer et al. (2015) using *Ks*-band photometry from the Two Micron All Sky Survey (T. H. Jarrett et al. 2003) to constrain the extended stellar light beyond the central $19\farcs2 \times 19\farcs2$ region. Within this region, the stellar-light distribution was derived from the HST Near Infrared Camera and Multi-Object Spectrometer F222M image (PID: 7230, PI: Scoville). The resulting surface-brightness model in terms of an MGE (E. Emsellem et al. 1994; M. Cappellari 2002), which consists of 12 concentric Gaussians, is listed in Table 1 of D. A. Drehmer et al. (2015), based on the MGE_FIT_SECTOR routine (M. Cappellari 2002).

To convert the *Ks*-band surface-brightness distribution into a stellar mass density model, we adopted the mass-follows-light assumption by scaling the MGE with a dynamical M/L in the *Ks* band (M/L_K). The dark matter fraction is expected to be completely negligible in the dense nuclear region of this galaxy. The MGE was analytically deprojected assuming a free inclination angle (i) to yield a three-dimensional axisymmetric mass density distribution. To account for the gravitational potential of the central SMBH, we approximated its mass distribution as a proper Keplerian potential by setting `analytic_los=False`. This is justified by the relatively large SOI of the SMBH in NGC 4258 (Section 3.6), which extends to a radius $\approx$4–5 times greater than the NIRSpec pixel scale and $\approx$2.5 times larger than the NIRSpec FWHM$_{\rm PSF}$.

3.2. Jeans Anisotropic Models

In this work, we investigate the impact of the axisymmetric gravitational potential under two extreme assumptions for the velocity ellipsoid alignment on the dynamical determination of the central $M_{\rm BH}$ in NGC 4258, using new stellar kinematic measurements from the NIRSpec G235H/F170LP data. We compare the JAM with cylindrically aligned velocity ellipsoids (JAM$_{\rm cyl}$; M. Cappellari 2008) and the version with spherically aligned velocity ellipsoids (JAM$_{\rm sph}$; M. Cappellari 2020).

The JAM$_{\rm cyl}$ model assumes a velocity ellipsoid aligned with cylindrical coordinates (R, ϕ, z), allowing for anisotropy in the 'vertical' z-direction, in which the vertical velocity dispersion differs from the equal radial and tangential dispersions ($\sigma_z \neq \sigma_R = \sigma_\phi$, velocity ellipsoid axially symmetric around the vertical direction: $\beta_z(R, z) = 1 - (\sigma_z/\sigma_R)^2$). In contrast, the JAM$_{\rm sph}$ model assumes a velocity ellipsoid aligned with spherical coordinates (r, θ, ϕ), allowing for anisotropy in the radial direction, in which the radial velocity dispersion is different from the equal azimuthal and tangential velocity dispersions ($\sigma_r \neq \sigma_\theta = \sigma_\phi$, or velocity ellipsoid axially symmetric around the radial direction: $\beta_r(r, \theta) = 1 - (\sigma_\theta/\sigma_r)^2$).

These JAM$_{\rm cyl}$ and JAM$_{\rm sph}$ models are achieved by setting the keyword `align='cyl'` to enforce cylindrical alignment and `align='sph'` to enforce spherical alignment in the `jam.axi.proj` procedure within the JAMPY package (M. Cappellari 2020),[18] approximating for the intrinsic second

[18] v7.2.0: https://pypi.org/project/jampy/

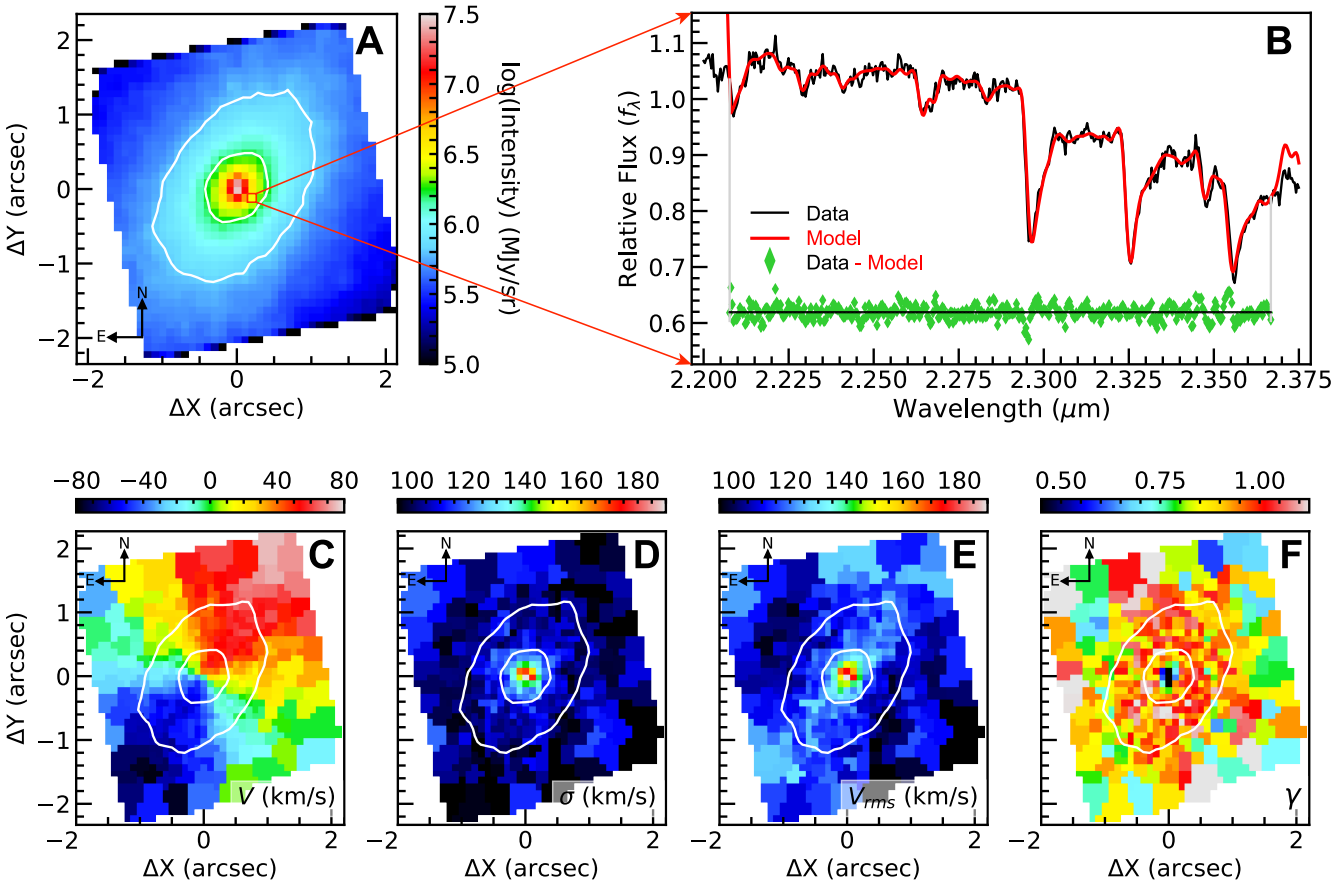

Figure 5. Stellar kinematics extracted from the JWST/NIRSpec G235H/F170LP IFU of NGC 4258 are presented. Panel (A): same as the left panel of Figure 2. Panel (B): a representative PPXF fit for a central-offset Voronoi bin that is unaffected by wiggle artifacts; its location is marked in panel (A). The observed spectrum, which includes the stellar CO bandhead absorption features at ∼2.3 μm, is shown in black, with the best-fit empirical XSL template overlaid in red. The fit residuals, `(data - model)`, are shown in green. The vertical gray lines indicate the spectral range used in fitting the templates to the spectra in all bins. Panels (C)–(F): maps of the stellar rotation velocity (V), velocity dispersion (σ), rms velocity ($V_{\rm rms} = \sqrt{V^2 + \sigma^2}$), and stellar-light contribution fraction (γ), respectively. White contours trace the intensity distribution, decreasing by 1 mag arcsec^{-2} from the center outward.

velocity moments (i.e., $\langle\sigma_z^2\rangle$ and $\langle\sigma_\phi^2\rangle$ for JAM$_{\rm cyl}$, or $\langle\sigma_r^2\rangle$ and $\langle\sigma_\theta^2\rangle$ for JAM$_{\rm sph}$). This approximation is purely a numerical convenience that allows for fast computation of the model predictions for JAM$_{\rm cyl}$, while the JAM$_{\rm sph}$ models always compute the black hole potential exactly.

3.3. Model Grid and Parameter Space

To model the stellar kinematics and dynamics of NGC 4258's nucleus, we compared the observed NIRSpec G235H/F170LP $V_{\rm rms}$ map with predictions from both the JAM$_{\rm cyl}$ and JAM$_{\rm sph}$ models. These models estimate $M_{\rm BH}$ (sampled logarithmically) and constrain additional parameters scaled linearly: the mass-to-light ratio (M/L_K), inclination (i; converted to $q_{\rm min}$), and orbital anisotropy. For JAM$_{\rm sph}$, we assumed radial anisotropy (β_r), parametrized as the ratio σ_θ/σ_r; for JAM$_{\rm cyl}$, we assumed vertical anisotropy (β_z), parametrized as σ_z/σ_R. In the JAM$_{\rm cyl}$ model, we adopted a constant anisotropy without priors. For the physically motivated JAM$_{\rm sph}$ model, we implemented the D. A. Simon et al. (2024) logistic anisotropy with specific priors (Section 3.5). These two limiting cases assume a velocity ellipsoid aligned either radially (JAM$_{\rm sph}$) or vertically (JAM$_{\rm cyl}$), which shapes the predicted LOSVD.

Table 2
JWST/NIRSpec Kinematic Data of the NGC 4258 Nucleus

ΔR.A. (arcsec)	ΔDecl. (arcsec)	V (km s^{-1})	ΔV (km s^{-1})	σ (km s^{-1})	$\Delta\sigma$ (km s^{-1})
−0.168	0.130	39.04	2.45	132.75	3.01
−0.085	0.185	18.58	2.48	139.92	3.07
−0.030	0.101	21.50	5.28	171.38	6.69
−0.114	0.047	36.20	3.56	156.29	4.47
0.054	0.156	−6.27	5.46	139.51	6.75
−0.001	0.240	4.54	2.64	136.65	3.27
0.025	0.018	−5.36	8.07	191.06	9.52
…	…	…	…	…	…

Note. A data copy of this table is also available on Zenodo at doi:10.5281/zenodo.17729122.

(This table is available in its entirety in machine-readable form in the online article.)

In addition to the two JAM models, we assessed the systematic uncertainties in the $M_{\rm BH}$ measurement of NGC 4258 using three synthetic JWST/NIRSpec G235H/F170LP PSFs (Table 1) and by testing both constant and varying M/L_K models (Section 3.4). In total, we performed 12 JAM model runs, as listed in Table 3, which together bracket the main sources of systematic uncertainty in our dynamical analysis and are summarized below:

Table 3
Summary of the Best-fitting Parameters and Formal Uncertainties for the 12 JAM Models

M/L_K	$\mathrm{FWHM}_{\mathrm{PSF}}^{\mathrm{tot}}$ (arcsec)	M_{BH} ($\times 10^7\ M_\odot$)	M/L_K ($M_\odot/L_\odot$)	$M/L_K^{0''}$ ($M_\odot/L_\odot$)	$M/L_K^{2''}$ ($M_\odot/L_\odot$)	q_{min}	σ_z/σ_R	$(\sigma_r/\sigma_\theta)_0$	$(\sigma_r/\sigma_\theta)_\infty$
(1)	(2)	(3)	(4)	(5)	(6)	(7)	(8)	(9)	(10)
$\mathrm{JAM_{cyl}}$ Models with Constant Anisotropy									
Constant	0.08	4.52 ± 0.15	4.45 ± 0.07	⋯	⋯	0.22 ± 0.05	0.97 ± 0.02	⋯	⋯
Constant	0.15	4.06 ± 0.18	4.63 ± 0.10	⋯	⋯	0.08 ± 0.05	0.98 ± 0.02	⋯	⋯
Constant	0.20	4.10 ± 0.14	4.50 ± 0.09	⋯	⋯	0.25 ± 0.06	1.00 ± 0.02	⋯	⋯
Varying	0.08	3.75 ± 0.19	⋯	5.74 ± 0.23	3.34 ± 0.20	0.28 ± 0.05	0.98 ± 0.02	⋯	⋯
Varying	0.15	3.36 ± 0.14	⋯	5.92 ± 0.21	3.42 ± 0.16	0.31 ± 0.05	0.99 ± 0.02	⋯	⋯
Varying	0.20	3.73 ± 0.17	⋯	5.54 ± 0.27	3.75 ± 0.22	0.36 ± 0.08	1.03 ± 0.02	⋯	⋯
$\mathrm{JAM_{sph}}$ Models with Radially Varying Logistic Anisotropy									
Constant	0.08	4.39 ± 0.40	3.54 ± 0.64	⋯	⋯	0.26 ± 0.04	⋯	0.94 ± 0.18	1.30 ± 0.23
Constant	0.15	4.27 ± 0.30	3.56 ± 0.25	⋯	⋯	0.26 ± 0.05	⋯	0.78 ± 0.10	1.30 ± 0.05
Constant	0.20	4.55 ± 0.44	3.38 ± 0.57	⋯	⋯	0.19 ± 0.05	⋯	0.66 ± 0.16	1.30 ± 0.23
Varying	0.08	3.70 ± 0.43	⋯	4.40 ± 0.97	2.96 ± 0.48	0.29 ± 0.25	⋯	1.00 ± 0.26	1.30 ± 0.23
Varying	0.15	3.42 ± 0.45	⋯	4.59 ± 1.01	3.00 ± 0.52	0.29 ± 0.05	⋯	1.00 ± 0.25	1.29 ± 0.22
Varying	0.20	4.28 ± 0.61	⋯	3.76 ± 0.94	3.17 ± 0.80	0.20 ± 0.06	⋯	0.74 ± 0.34	1.30 ± 0.26

Notes. Column (1): assumed M/L_K profile type. Column (2): total FWHM of the synthetic PSF model. Column (3): best-fit black hole mass. Column (4): best-fit constant M/L_K. Columns (5) and (6): best-fit central and outer M/L_K for the varying profile. Column (7): best-fit intrinsic axial ratio. Column (8): best-fit vertical anisotropy for $\mathrm{JAM_{cyl}}$ models. Column (9): best-fit central radial anisotropy for $\mathrm{JAM_{sph}}$ models. Column (10): best-fit outer radial anisotropy for $\mathrm{JAM_{sph}}$ models.

1. *Anisotropy alignment (two options).* Either cylindrically aligned velocity ellipsoid ($\mathrm{JAM_{cyl}}$) or spherically aligned ($\mathrm{JAM_{sph}}$).
2. *Point-spread function (three options).* Three `stpsf` synthetic JWST/NIRSpec PSFs were tested (Table 1).
3. *Mass-to-light ratio (two options).* Either a constant M/L_K or a radially varying M/L_K (Section 3.4).

3.4. Linearly Varying M/L_K Profile

C. Siopis et al. (2009) demonstrated that the color gradient in the outer disk of NGC 4258 ($r > 2''$) is negligible. As shown in their Figure 4, there is no significant difference among the surface-brightness profiles in the V, R, and K bands extracted along the galaxy's photometric major axis after correcting for dust lanes and AGN contamination. This suggests that M/L_K remains constant beyond $2''$, i.e., $M/L_K(r \geqslant 2'') = M/L_K^{2''}$. However, within this radius the presence of nonthermal AGN emission likely causes a variation in M/L_K profile toward the galaxy center, which we model by allowing for a different nuclear mass-to-light ratio $M/L_K^{0''}$. We thus performed alternative JAM tests assuming a radially varying $M/L_K(r)$, which changes linearly from $r = 0''$ to $r = 2''$ and remains constant outside this interval.

In JAMs, the $M/L_K(r)$ profile is implemented by associating a different $(M/L_K)_j$ to each Gaussian component with dispersion σ_j in the MGE listed in Table 1 of D. A. Drehmer et al. (2015), as follows:

$$(M/L_K)_j = \begin{cases} M/L_K^{0''} + \dfrac{M/L_K^{2''} - M/L_K^{0''}}{2''} \times \sigma_j, & \sigma_j < 2'' \\ M/L_K^{2''}, & \sigma_j \geqslant 2'' \end{cases}. \quad (1)$$

3.5. Logistic Anisotropy for $\mathrm{JAM_{sph}}$ Models

We further explored the $\mathrm{JAM_{sph}}$ model using a radially varying anisotropy (D. A. Simon et al. 2024), obtained using the `logistic` keyword in $\mathrm{JAM_{sph}}$, to investigate how the stellar orbital structure changes across the nuclear region of NGC 4258 by adopting the logistic function of $\log r$ below:

$$\beta_r(r) = \beta_{r,0} + \frac{\beta_{r,\infty} - \beta_{r,0}}{1 + (r_a/r)^\alpha}. \quad (2)$$

Here, r_a is the transition radius at which the stellar motion changes from being dominated by $\beta_{r,0}$ to $\beta_{r,\infty}$, which represent the anisotropy parameters at the center and at large radii, respectively. These parameters relate to the ratio of stellar velocity dispersions in the radial and azimuthal directions at the corresponding locations as

$$(\sigma_r/\sigma_\theta)_0 = \frac{1}{\sqrt{1 - \beta_{r,0}}} \quad \text{and} \quad (\sigma_r/\sigma_\theta)_\infty = \frac{1}{\sqrt{1 - \beta_{r,\infty}}}.$$

We applied specific priors $0.5 < (\sigma_r/\sigma_\theta)_0 < 1$ and $1 < (\sigma_r/\sigma_\theta)_\infty < 1.3$ to constrain the inner and outer anisotropies, as suggested in D. A. Simon et al. (2024, Table 3). Moreover, the anisotropy transition radius r_a was restricted to lie between the range of $r_{\mathrm{SOI}} < r_a < 1''$ to prevent the model from becoming radially anisotropic within r_{SOI}. Additionally, we fixed the sharpness parameter to $\alpha = 2$ to reduce the dimension of parameter space and reduce degeneracies, given the weak dependence of the results on the choice of this parameter.

3.6. Markov Chain Monte Carlo Fitting and Uncertainty Estimation

We determine the SMBH mass, M_{BH}, and other model parameters by performing a Markov Chain Monte Carlo

(MCMC) analysis for each JAM model. To explore the parameter space, we employ the adaptive Metropolis algorithm (H. Haario et al. 2001) as implemented in the ADAMET code (M. Cappellari et al. 2013).[19]

For each model, we generate a chain of 10^5 steps. We discard the initial 20% as the burn-in phase and use the remaining samples to construct the posterior probability distributions. The most probable parameter values are taken as the maximum of the likelihood, with uncertainties derived from the 1σ (16th–84th percentile) and 3σ (0.14th–99.86th percentile) confidence intervals of the marginalized posteriors.

Dynamical modeling of numerous high-precision kinematic data points, as in our case, presents two well-known challenges:

1. *Underestimated uncertainties.* The formal statistical errors on derived parameters can become unrealistically small, often dwarfed by unmodeled systematic effects.
2. *Dominance of large-radii data.* The χ^2 statistic can be disproportionately influenced by the large number of data points at large radii. This risks biasing the $M_{\rm BH}$ measurement, which should be dictated primarily by the kinematics within the black hole's SOI.

To mitigate the first issue, we adopt an error inflation scheme. We base our approach on the heuristic $\Delta\chi^2$-increase method of R. C. E. van den Bosch & G. van de Ven (2009), which in a Bayesian framework is equivalent to inflating the kinematic measurement errors by a factor of $(2N)^{1/4}$, where N is the number of data points (M. Mitzkus et al. 2017, Section 6.1). While this technique is now standard for Atacama Large Millimeter/submillimeter Array (ALMA)-based $M_{\rm BH}$ measurements (e.g., M. D. Smith et al. 2019; D. D. Nguyen et al. 2020, 2021, 2022; H. N. Ngo et al. 2025), a uniform inflation across all radii does not resolve the second challenge.

Therefore, we apply the inflation selectively. We preserve the formal kinematic uncertainties for all data points inside the SOI ($r \leqslant r_{\rm SOI} \approx 0\farcs45$), where the SMBH's gravitational potential dominates. For the $N_{r>r_{\rm SOI}} = 338$ kinematic bins outside this radius, we inflate their associated errors by a factor of $(2N_{r>r_{\rm SOI}})^{1/4}$. This refined strategy ensures the $M_{\rm BH}$ determination is driven by the central kinematics, while still accounting for potential systematic errors at larger radii. This selective approach has been successfully employed in previous dynamical studies using IFU data from Gemini/NIFS (D. A. Drehmer et al. 2015) and MUSE (S. Thater et al. 2022, Section 4.3).

4. Results and Discussion

We summarize in Table 3 the best-fit parameters and their 1σ uncertainties for the 12 JAM models used to fit the NIRSpec G235H/F170LP $V_{\rm rms}$ data. Across all model assumptions, the inferred $M_{\rm BH}$ ranges from (3.36–4.55) $\times$ $10^7\,M_\odot$, and the M/L_K values span (3.38–4.63) $M_\odot/L_\odot$. While both $M_{\rm BH}$ and M/L_K are relatively insensitive to the choice of PSF, they are more strongly affected by the assumed velocity ellipsoid alignment. Specifically, the $\rm JAM_{cyl}$ models yield $M_{\rm BH}$ and M/L_K values that are approximately 23% higher than those from the $\rm JAM_{sph}$ models. In addition, the inferred $q_{\rm min}$ values range from 0.19 to 0.36, corresponding to inclination angles of $i \sim$ (65–73)°.

Figure 6 presents the $V_{\rm rms}$ profiles of all 12 best-fitting JAM models (with their 1σ uncertainties), extracted along the major and minor axes of NGC 4258. These are compared directly to the observed $V_{\rm rms}$ profiles from the NIRSpec G235H/F170LP data, extracted in the same way. All models generally provide a good match to the data and to one another across the NIRSpec FOV, despite differing assumptions of the M/L_K profile and orbital anisotropy. A systematic offset is seen at the very center, corresponding to the innermost kinematic bins, likely due to differences in the treatment of our synthetic NIRSpec PSF in the modeling (Section 2.3 and Table 1). In particular, models assuming PSF 3 ($\rm FWHM_{PSF,tot} \approx 0\farcs2$) fail to reproduce the central $V_{\rm rms}$ values, missing by $\approx$20 km s^{-1} (see right-hand column of Figure 6). In contrast, the best-fitting models using PSF 1 ($\rm FWHM_{PSF,tot} \approx 0\farcs08$; left-hand column) and PSF 2 ($\rm FWHM_{PSF,tot} \approx 0\farcs15$; middle column) yield a significantly better fit to the G235H/F170LP data. Although the JAM models using our synthetic PSF 1 provide the best match to the $V_{\rm rms}$ data, including the innermost bins, those based on synthetic PSF 2 match the central data within the 1σ $V_{\rm rms}$ uncertainties. We prefer the best-fit parameters from the models using synthetic PSF 2, as its total FWHM closely matches that of the empirically determined PSF from F. D'Eugenio et al. (2024, 2026).

Our 12 JAM runs provide an ensemble of broadly acceptable models spanning a range of assumptions and systematic effects. This approach allows us to move beyond the common practice of relying on the unreliable formal uncertainties from a single "preferred" model and instead compute robust ensemble statistics. The mean black hole mass from our 12 models is $(4.01 \pm 0.12) \times 10^7\,M_\odot$, where the uncertainty is the standard error of the mean. However, the mean relies on the assumption that the distribution of model results is Gaussian, which may not be the case, and its uncertainty may be unrealistically small. We therefore also compute a more robust estimate, the median with its bootstrap 68% (1σ) confidence intervals, which yields $M_{\rm BH} = (4.08^{+0.19}_{-0.33}) \times 10^7\,M_\odot$. We adopt this median value as our final, more robust estimate, in part because of its slightly larger and more conservative uncertainty. Both the mean and median values are consistent with the benchmark maser value within their uncertainties. Our adopted mass is just 5% larger than the maser-based value of $(3.9 \pm 0.1) \times 10^7\,M_\odot$ (J. R. Herrnstein et al. 1999), 15% smaller than the previous JAM stellar-dynamical estimate of $(4.8 \pm 0.3) \times 10^7\,M_\odot$ from D. A. Drehmer et al. (2015, converted to 1σ confidence), and 24% larger than the Schwarzschild model value of $(3.3 \pm 0.2) \times 10^7\,M_\odot$ from C. Siopis et al. (2009).

The best-fit $\rm JAM_{cyl}$ models are generally isotropic, with constrained values of $\sigma_z/\sigma_R \sim 1$ (i.e., $\beta_z \sim 0$), regardless of whether a constant or varying M/L_K is assumed. In contrast, the derived $M_{\rm BH}$ shows a stronger dependence on the assumed M/L_K profile in the nucleus of NGC 4258: $M_{\rm BH}$ values are 6%–18% higher or 2%–12% lower than the maser-based $M_{\rm BH}$ (J. R. Herrnstein et al. 1999) under constant or linearly varying M/L_K assumptions, respectively. These smaller $M_{\rm BH}$ values, constrained from the linearly varying M/L_K profile, result from its negative slope. A similar trend in the dependence of the constrained $M_{\rm BH}$ on the assumed M/L_K profile is also observed in the best-fit $\rm JAM_{sph}$ models with logistic anisotropy. This result suggests the possible presence of dust within the NIRSpec IFU FOV of NGC 4258, contributing nonthermal light similar to AGN emission, but at larger radii beyond the

[19] v2.0.9: https://pypi.org/project/adamet/

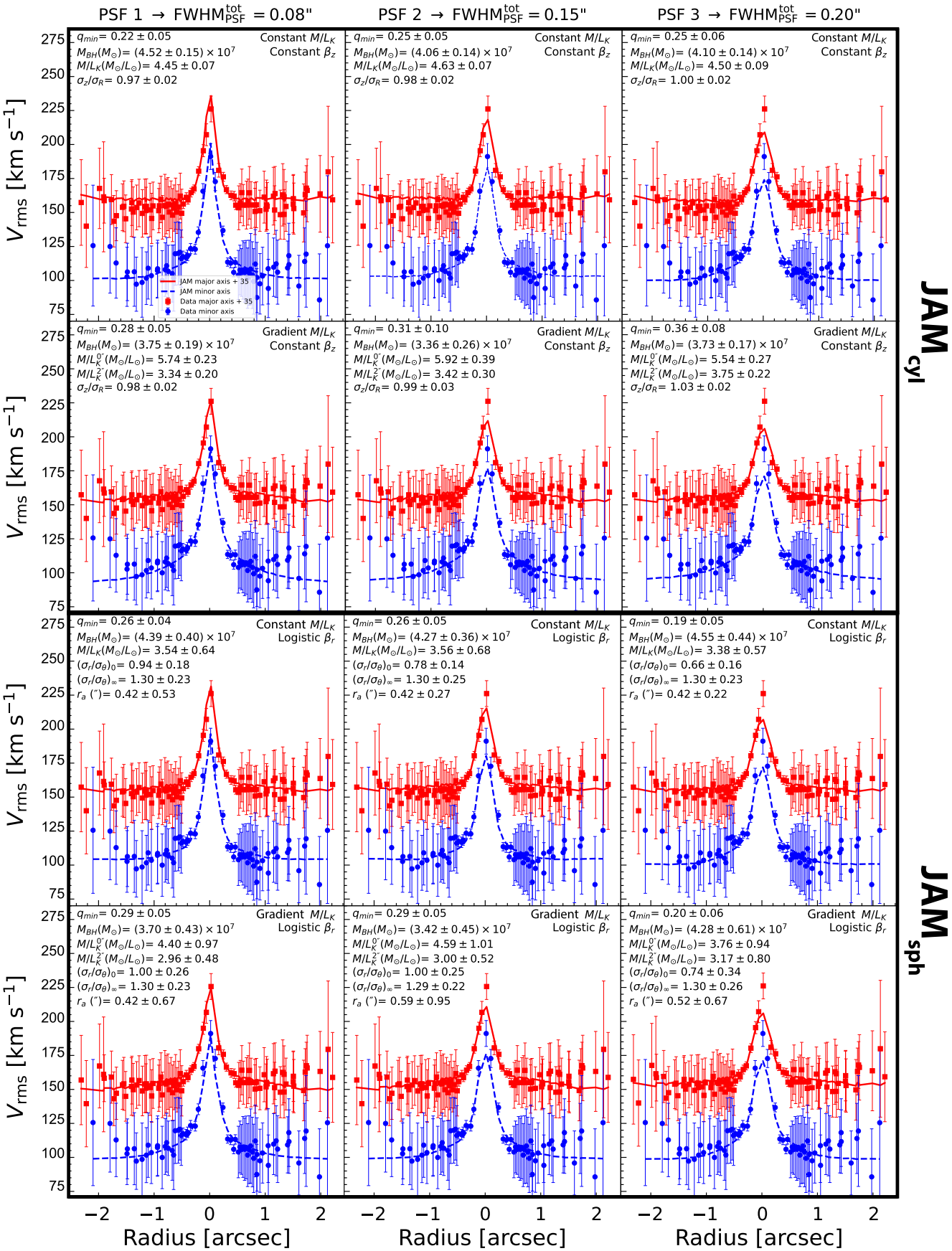

Figure 6. Stellar kinematics extracted from the NIRSpec G235H/F170LP data cube are shown as filled red (major axis + 35 km s^{-1}) and blue (minor axis) points, overlaid with best-fit JAM models assuming various combinations of M/L_K and orbital anisotropy. Each model includes its corresponding best-fit parameters and associated 1σ uncertainties in the legend.

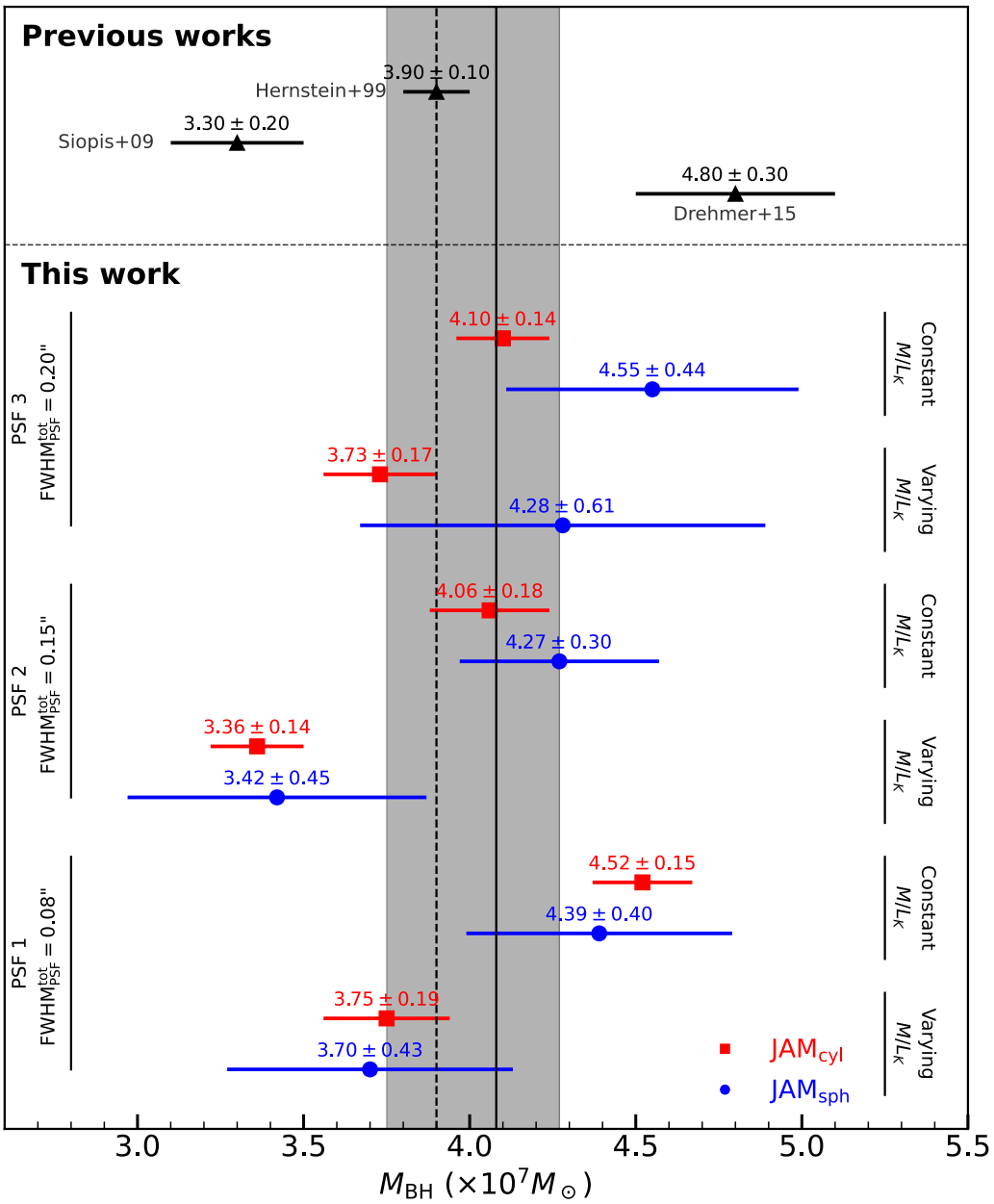

Figure 7. Black hole mass measurements and their 1σ uncertainties for NGC 4258 are shown from our 12 JAM model runs based on the NIRSpec G235H/F170LP data cube, compared with previous dynamical estimates from "gold-standard" masers (vertical dashed line; J. R. Herrnstein et al. 1999), stars (C. Siopis et al. 2009; D. A. Drehmer et al. 2015), and gas (G. Pastorini et al. 2007). The legend indicates the results from our JAM models under different assumptions for the NIRSpec PSF, stellar velocity anisotropy, and M/L_K profiles. Our adopted M_{BH} is shown as the vertical solid line, with the gray band indicating the ensemble median and 68% (1σ) bootstrap confidence interval from all 12 JAM models.

galaxy center. This supports our inference of a spatially varying stellar-light fraction, $\gamma < 1$, especially elongated along the minor axis as shown in panel (F) of Figure 5.

In Figure 7, we present our 12 M_{BH} measurements alongside the benchmark water-maser result (J. R. Herrnstein et al. 1999) and stellar-dynamical estimates from HST/STIS (C. Siopis et al. 2009) and Gemini/NIFS (D. A. Drehmer et al. 2015). Uncertainties are shown as error bars, providing a clear, presentation-ready summary of this benchmark extragalactic constraint on M_{BH} in NGC 4258. The left panel of Figure 8 shows example 2D posterior distributions for each model parameter of the JAM$_{cyl}$ model with constant M/L_K, constant anisotropy, and PSF 2. Point colors indicate the relative likelihood (white denotes the maximum likelihood and 1σ, and black marks the 3σ confidence levels, CLs). The accompanying one-dimensional histograms are used to derive the best-fit values and 1σ uncertainties, which reflect the propagation of stellar kinematics and random errors. All four parameters are well constrained. The figure also illustrates the agreement between the observed V_{rms} and that predicted by the best-fit JAM$_{cyl}$ model.

Similarly, in the right panel of Figure 8, we show the 2D posterior distributions for each model parameter of the JAM$_{sph}$ model with constant M/L_K, logistic anisotropy, and PSF 2. The posterior distributions for the JAM$_{sph}$ model appear to hit the boundary set by our anisotropy prior, indicating that certain parameters are only weakly constrained by the data alone and are partially driven by the

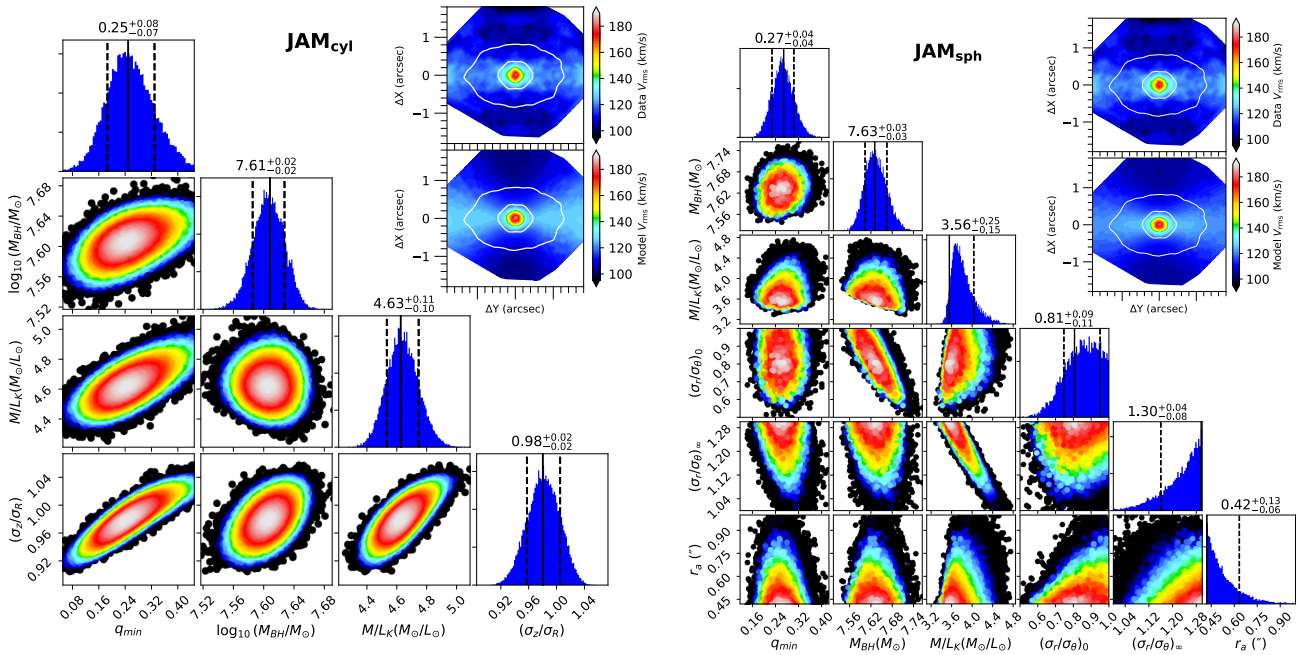

Figure 8. Left: posterior distributions for the JAM$_{\rm cyl}$ model with constant M/L_K and anisotropy, obtained after the burn-in phase of the ADAMET MCMC optimization, are shown for the nucleus stellar kinematics of NGC 4258 from the NIRSpec G235H/F170LP data. The triangle plot displays the 2D projected probability distributions of the model parameters ($q_{\rm min}$, $M_{\rm BH}$, M/L_K, σ_z/σ_R), with one-dimensional marginalized histograms along the diagonal. Solid vertical lines mark the best-fit values, while dashed lines indicate the 1σ uncertainties. Inset panels in the upper right compare the observed and model-predicted $V_{\rm rms}$ using a constant velocity scale. Both $V_{\rm rms}$ maps were symmetrized under the assumption of axisymmetry and reoriented with the major and minor axes aligned along the horizontal and vertical directions, respectively, using the SYMMETRIZE_VELFIELD routine from the PLOTBIN (v3.1.7; https://pypi.org/project/plotbin/) package. Both the symmetrized data and model prediction were visualized using PLOT_VELFIELD. The strong agreement across the NIRSpec FOV confirms the model's fidelity. Right: same as the left panel, but applying the JAM$_{\rm sph}$ models with logistic varying β_r profile and the model parameters ($q_{\rm min}$, $M_{\rm BH}$, M/L_K, $(\sigma_r/\sigma_\theta)_0$, $(\sigma_r/\sigma_\theta)_\infty$, r_a).

priors. We emphasize that this behavior is expected and, in fact, necessary. In galaxy dynamics analyses of single galaxies, observational data are often insufficient to uniquely constrain all model parameters due to intrinsic degeneracies, such as the well-known mass–anisotropy degeneracy (J. Binney & G. A. Mamon 1982). If the posterior distributions were entirely unaffected by the priors, it would imply that the priors were unnecessary. Instead, the priors serve their intended purpose: to incorporate external physical knowledge—accumulated over decades of dynamical modeling studies—to break degeneracies that the data cannot resolve on their own. Often priors are assumed to be Gaussian, and their influence on the posterior is not as obvious as when priors are set as sharp boundaries, as we do here. However, in either case, priors affect the posterior, and the ability to enforce them is an integral feature and a key strength of the Bayesian approach. The JAM method is particularly well suited to enforcing priors, which have always been a key feature of its applications. This approach is superior to assuming complete ignorance (flat priors), which can lead to unphysical solutions, as historically demonstrated by the extreme anisotropy required to explain the kinematics of M87 without a black hole (J. Binney & G. A. Mamon 1982). By leveraging informative priors, we ensure that our $M_{\rm BH}$ estimates remain robust and physically consistent with our current understanding of galaxy structure.

Figure 9 illustrates a set of 100,000 anisotropy profiles randomly drawn from the 2D posterior distributions in the right panel of Figure 8. These profiles exhibit a radially increasing trend, often found in galaxy centers (J. Thomas et al. 2014; M. Cappellari 2026, Figure 10 in that paper).

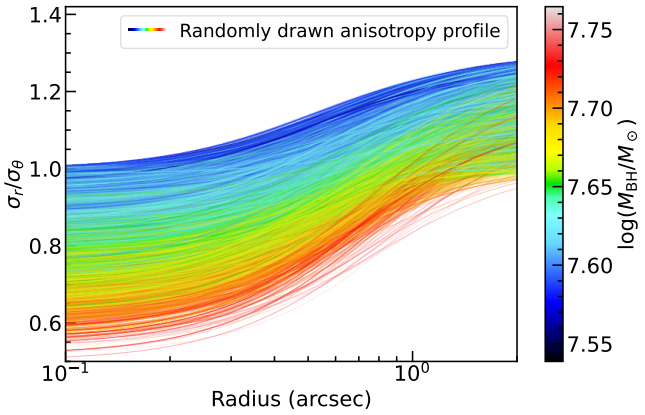

Figure 9. Plot of 100,000 anisotropy profiles randomly sampled from the MCMC chain, color-coded by their corresponding $M_{\rm BH}$ values. The profiles show clear evidence of a radially increasing anisotropy ratio, though they exhibit significant variation due to the mass–anisotropy degeneracy.

Notably, the profiles tend to transition from roughly constant values at larger radii to lower values near $\approx 0\farcs42$–$0\farcs6$. This transition scale is close to the black hole's SOI in NGC 4258, where stellar random motions are strongly enhanced by the black hole's gravitational potential, resulting in tangential anisotropy. Beyond the SOI, the anisotropy gradually shifts toward radially dominated stellar motions. We observe a strong $M_{\rm BH}$–anisotropy degeneracy, in which higher $M_{\rm BH}$ values correspond to more tangential velocity anisotropy, while lower $M_{\rm BH}$ values correspond to more radial anisotropy, consistent with that observed in the core elliptical galaxy M87 (Figure 15 of D. A. Simon et al. 2024).

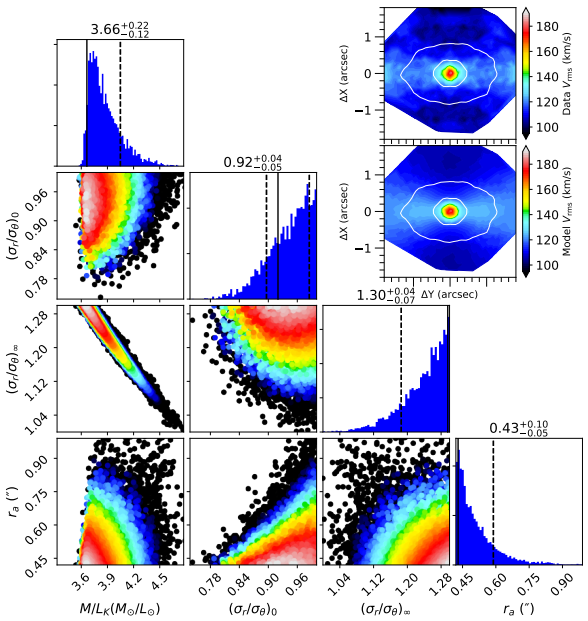

Figure 10. Same as Figure 8, but for the $\mathrm{JAM_{sph}}$ models with the M_{BH} fixed to the maser-based estimate from J. R. Herrnstein et al. (1999) and the inclination fixed to that of the best-fitting $\mathrm{JAM_{sph}}$ model.

Within the 3σ CL region of the 2D posterior distributions, we find no significant covariance between M_{BH} and M/L_K in the JAM models, indicating that both parameters are well constrained. Additionally, a positive covariance is observed between M/L_K and the orbital anisotropy parameter (i.e., σ_θ/σ_r in the $\mathrm{JAM_{sph}}$ model and σ_z/σ_R in the $\mathrm{JAM_{cyl}}$ model), suggesting that variations in anisotropy can partially compensate for changes in M/L_K during the fitting process.

Given that the water-maser-based M_{BH} measurement from J. R. Herrnstein et al. (1999) remains the most accurate extragalactic determination, we tested a $\mathrm{JAM_{sph}}$ model with constant M/L_K, logistic anisotropy, and PSF 2, in which M_{BH} was fixed to this value and q_{min} was set to that of the best-fitting $\mathrm{JAM_{sph}}$ model, while allowing M/L_K, r_a, and the $(\sigma_r/\sigma_\theta)_0$ and $(\sigma_r/\sigma_\theta)_\infty$ ratios to vary freely. As shown in Figure 10, we find a strong anti-covariance between M/L_K and $(\sigma_r/\sigma_\theta)_\infty$, reflecting the M_{BH}–anisotropy degeneracy. The best-fit M/L_K remains fully consistent with that of the original $\mathrm{JAM_{sph}}$ model. For smaller black hole masses, the anisotropy becomes less tangential and more radial, with $(\sigma_r/\sigma_\theta)_0$ increasing by 12%.

Our stellar-based M_{BH} constraints, derived under both cylindrical and spherical velocity ellipsoid assumptions, yield $r_{\mathrm{SOI}} \approx 0\farcs45$ (or 16 pc). These radii are ≈2–3 times larger than the spatial resolution of the JWST observations, demonstrating that our M_{BH} estimates are robust and spatially well resolved. The kinematic signature of the SMBH is clearly detected within the central ≈55 spaxels.

5. Conclusions

We have measured the SMBH mass in the benchmark galaxy NGC 4258 using high-resolution 2D stellar kinematics from JWST/NIRSpec IFU observations. By applying JAM models to the stellar velocity distribution derived from the CO bandheads, we robustly determined the central dark mass. Our main findings are summarized as follows:

1. We successfully recovered the stellar kinematics by separating the stellar light from the nonthermal AGN continuum, which contributes up to 56% of the flux in the central spaxel. This was achieved by fitting a fixed optimal stellar template combined with additive and multiplicative polynomials to model the AGN contribution.
2. The resulting kinematic maps show clear rotation ($\pm 80\,\mathrm{km\,s^{-1}}$) and a sharp increase in velocity dispersion toward the center, peaking at $191 \pm 12\,\mathrm{km\,s^{-1}}$. This central kinematic spike is a clear signature of the SMBH's gravitational influence and is resolved by the NIRSpec data.
3. We ran a grid of 12 JAM models to explore systematic uncertainties from the PSF, M/L profile, and orbital anisotropy. The ensemble median and corresponding bootstrap 68% (1σ) confidence interval of these models yields a black hole mass of $M_{\mathrm{BH}} = (4.08^{+0.19}_{-0.33}) \times 10^7\ M_\odot$. This result, which incorporates both statistical and systematic uncertainties, is in excellent agreement with the precise maser-based mass.
4. Our analysis shows that the choice of PSF significantly impacts the fit quality. Models using a synthetic PSF with a FWHM of 0.″15 provide the best match to the central kinematics, consistent with recent empirical PSF measurements for NIRSpec.
5. This work demonstrates that JWST/NIRSpec stellar kinematics can deliver precise and accurate SMBH masses, even in AGN-dominated nuclei. Our result for NGC 4258 validates the stellar-dynamical method against the gold-standard maser technique, paving the way for robust mass measurements in more distant galaxies.

Acknowledgments

The authors would like to thank the anonymous referee for their careful reading and useful comments, which helped to improve the paper greatly. Research conducted by T.N.L. is partially supported by a grant from the Simons Foundation to IFIRSE, ICISE (916424, N.H.). N.T. would like to acknowledge partial support from the UKRI grant No. ST/X002322/1 for UK ELT Instrument Development at Oxford. M.P. acknowledges support through grant Nos. PID2021-127718NB-I00 and RYC2023-044853-I, funded by the Spanish Ministry of Science and Innovation/State Agency of Research MCIN/AEI/10.13039/501100011033 and El Fondo Social Europeo Plus FSE+. M.P.S. acknowledges support under grant Nos. RYC2021-033094-I, CNS2023-145506, and PID2023-146667NB-I00, funded by MCIN/AEI/10.13039/501100011033 and the European Union NextGenerationEU/PRTR.

This research is based on observations made with the NASA/ESA Hubble Space Telescope obtained from the Space Telescope Science Institute, which is operated by the Association of Universities for Research in Astronomy, Inc., under NASA contract NAS 5-26555. This work is based (in part) on observations made with the NASA/ESA/CSA James Webb Space Telescope. The data were obtained from the Mikulski Archive for Space Telescopes at the Space Telescope Science Institute, which is operated by the Association of

Universities for Research in Astronomy, Inc., under NASA contract NAS 5-03127 for JWST. These observations are associated with program #02016.

Some/all of the data presented in this article were obtained from the Mikulski Archive for Space Telescopes (MAST) at the Space Telescope Science Institute. The specific observations analyzed can be accessed via doi:10.17909/baxx-nf29.

Facility: JWST.

Software: `Python v3.12` (G. Van Rossum & F. L. Drake 2009), `Matplotlib v3.6` (J. D. Hunter 2007), `NumPy v1.22` (C. R. Harris et al. 2020), `SciPy v1.3` (P. Virtanen et al. 2020), `photutils v0.7` (L. Bradley et al. 2024), `AstroPy v5.1` (Astropy Collaboration et al. 2022), `AdaMet v2.0` (M. Cappellari et al. 2013), `JamPy v7.2` (M. Cappellari 2020), `pPXF v8.2` (M. Cappellari 2023), `vorbin v3.1` (M. Cappellari & Y. Copin 2003), `MgeFit v5.0` (M. Cappellari 2002).

ORCID iDs

Dieu D. Nguyen https://orcid.org/0000-0002-5678-1008
Hai N. Ngo https://orcid.org/0009-0006-5852-4538
Michele Cappellari https://orcid.org/0000-0002-1283-8420
Tinh Q. T. Le https://orcid.org/0009-0004-3689-8577
Tien H. T. Ho https://orcid.org/0009-0005-8845-9725
Elena Gallo https://orcid.org/0000-0001-5802-6041
Niranjan Thatte https://orcid.org/0000-0002-6694-5184
Fan Zou https://orcid.org/0000-0002-4436-6923
Michele Perna https://orcid.org/0000-0002-0362-5941
Miguel Pereira-Santaella https://orcid.org/0000-0002-4005-9619

References

Ahn, C. P., Seth, A. C., Cappellari, M., et al. 2018, ApJ, 858, 102
Astropy Collaboration, Price-Whelan, A. M., Lim, P. L., et al. 2022, ApJ, 935, 167
Binney, J., & Mamon, G. A. 1982, MNRAS, 200, 361
Bradley, L., Sipőcz, B., Robitaille, T., et al. 2024, astropy/photutils: v2.0.2, Zenodo, doi:10.5281/zenodo.13989456
Cappellari, M. 2002, MNRAS, 333, 400
Cappellari, M. 2008, MNRAS, 390, 71
Cappellari, M. 2017, MNRAS, 466, 798
Cappellari, M. 2020, MNRAS, 494, 4819
Cappellari, M. 2023, MNRAS, 526, 3273
Cappellari, M. 2026, Encyclopedia of Astrophysics, Vol. 4 (Elsevier), 122
Cappellari, M., & Copin, Y. 2003, MNRAS, 342, 345
Cappellari, M., & Emsellem, E. 2004, PASP, 116, 138
Cappellari, M., Neumayer, N., Reunanen, J., et al. 2009, MNRAS, 394, 660
Cappellari, M., Scott, N., Alatalo, K., et al. 2013, MNRAS, 432, 1709
Davis, T. A., Nguyen, D. D., Seth, A. C., et al. 2020, MNRAS, 496, 4061
D'Eugenio, F., Juodžbalis, I., Ji, X., et al. 2026, MNRAS, 545, staf2117
D'Eugenio, F., Pérez-Gonzáalez, P. G., Maiolino, R., et al. 2024, NaAs, 8, 1443
Drehmer, D. A., Storchi-Bergmann, T., Ferrari, F., Cappellari, M., & Riffel, R. A. 2015, MNRAS, 450, 128
Emsellem, E., Monnet, G., & Bacon, R. 1994, A&A, 285, 723
Genzel, R., Thatte, N., Krabbe, A., Kroker, H., & Tacconi-Garman, L. E. 1996, ApJ, 472, 153
Gerhard, O. E. 1993, MNRAS, 265, 213
Ghez, A. M., Klein, B. L., Morris, M., & Becklin, E. E. 1998, ApJ, 509, 678
Haario, H., Saksman, E., & Tamminen, J. 2001, Bernoulli, 7, 223
Harris, C. R., Millman, K. J., van der Walt, S. J., et al. 2020, Natur, 585, 357
Herrnstein, J. R., Moran, J. M., Greenhill, L. J., & Trotter, A. S. 2005, ApJ, 629, 719
Herrnstein, J. R., Moran, J. M., Greenhill, L. J., et al. 1999, Natur, 400, 539
Hoaglin, D. C., Mosteller, F., & Tukey, J. W. 1983, Understanding Robust and Exploratory Data Analysis (Wiley)
Hunter, J. D. 2007, CSE, 9, 90
Husser, T.-O., Wende-von Berg, S., Dreizler, S., et al. 2013, A&A, 553, A6
Jarrett, T. H., Chester, T., Cutri, R., Schneider, S. E., & Huchra, J. P. 2003, AJ, 125, 525
Krajnović, D., Cappellari, M., de Zeeuw, P. T., & Copin, Y. 2006, MNRAS, 366, 787
Law, D. R., E. Morrison, J., Argyriou, I., et al. 2023, AJ, 166, 45
Marconi, A., Schreier, E. J., Koekemoer, A., et al. 2000, ApJ, 528, 276
Mitzkus, M., Cappellari, M., & Walcher, C. J. 2017, MNRAS, 464, 4789
Miyoshi, M., Moran, J., Herrnstein, J., et al. 1995, Natur, 373, 127
Ngo, H. N., Nguyen, D. D., Le, T. Q. T., et al. 2025, ApJ, 992, 211
Nguyen, D. D. 2017, arXiv:1712.02470
Nguyen, D. D., Bureau, M., Thater, S., et al. 2022, MNRAS, 509, 2920
Nguyen, D. D., Cappellari, M., Ngo, H. N., et al. 2025a, AJ, 170, 124
Nguyen, D. D., Cappellari, M., & Pereira-Santaella, M. 2023, MNRAS, 526, 3548
Nguyen, D. D., den Brok, M., Seth, A. C., et al. 2020, ApJ, 892, 68
Nguyen, D. D., Izumi, T., Thater, S., et al. 2021, MNRAS, 504, 4123
Nguyen, D. D., Ngo, H. N., Le, T. Q. T., et al. 2025b, A&A, 698, L9
Nguyen, D. D., Seth, A. C., den Brok, M., et al. 2017, ApJ, 836, 237
Nguyen, D. D., Seth, A. C., Neumayer, N., et al. 2018, ApJ, 858, 118
Nguyen, D. D., Seth, A. C., Neumayer, N., et al. 2019, ApJ, 872, 104
Nguyen, D. D., Seth, A. C., Reines, A. E., et al. 2014, ApJ, 794, 34
Pastorini, G., Marconi, A., Capetti, A., et al. 2007, A&A, 469, 405
Perna, M., Arribas, S., Marshall, M., et al. 2023, A&A, 679, A89
Perrin, M., Long, J., Osborne, S., et al. 2025, STPSF, v2.1.0, Zenodo, doi:10.5281/zenodo.15747364
Schwarzschild, M. 1979, ApJ, 232, 236
Silge, J. D., & Gebhardt, K. 2003, AJ, 125, 2809
Simon, D. A., Cappellari, M., & Hartke, J. 2024, MNRAS, 527, 2341
Siopis, C., Gebhardt, K., Lauer, T. R., et al. 2009, ApJ, 693, 946
Smith, M. D., Bureau, M., Davis, T. A., et al. 2019, MNRAS, 485, 4359
Tahmasebzadeh, B., Taylor, M. A., Valluri, M., et al. 2025, ApJL, 989, L42
Taylor, M. A., Tahmasebzadeh, B., Thompson, S., et al. 2025, ApJL, 991, L24
Thater, S., Krajnović, D., Weilbacher, P. M., et al. 2022, MNRAS, 509, 5416
Thater, S., Lyubenova, M., Fahrion, K., et al. 2023, A&A, 675, A18
Thomas, J., Saglia, R. P., Bender, R., Erwin, P., & Fabricius, M. 2014, ApJ, 782, 39
van den Bosch, R. C. E., & van de Ven, G. 2009, MNRAS, 398, 1117
van der Marel, R. P. 1994, MNRAS, 270, 271
van der Marel, R. P., & Franx, M. 1993, ApJ, 407, 525
Van Rossum, G., & Drake, F. L. 2009, Python 3 Reference Manual (CreateSpace)
Verro, K., Trager, S. C., Peletier, R. F., et al. 2022, A&A, 660, A34
Virtanen, P., Gommers, R., Oliphant, T. E., et al. 2020, NatMe, 17, 261
Wilkes, B. J., Schmidt, G. D., Smith, P. S., Mathur, S., & McLeod, K. K. 1995, ApJL, 455, L13